Chemical Engineering Journal 283 (2016) 1244–1253

Contents lists available at ScienceDirect

Chemical Engineering Journal

journal homepage: www.elsevier.com/locate/cej

Synthesis, characterization and visible light photocatalytic activity of metal based TiO_2 monoliths for CO_2 reduction

Oluwafunmilola Ola *, M. Mercedes Maroto-Valer

Centre for Innovation in Carbon Capture and Storage (CICCS), School of Engineering and Physical Sciences, Heriot-Watt University, Edinburgh EH14 4AS, United Kingdom

HIGHLIGHTS

- Coated monolithic structures were tested for visible-light-induced CO_2 reduction.
- Red shift in absorption edge was observed with increasing metal concentration.
- Fuel production rate is enhanced upon chromium, vanadium or cobalt deposition.

GRAPHICAL ABSTRACT

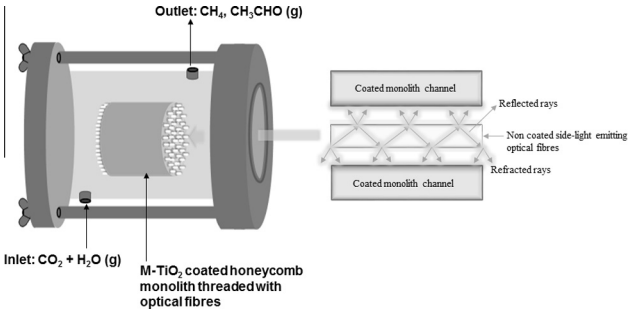

ARTICLE INFO

Article history:
Received 8 April 2015
Received in revised form 21 July 2015
Accepted 28 July 2015
Available online 28 August 2015

Keywords:
Visible light
Photocatalysis
Ceramic monoliths
Titanium dioxide
Optical fibres
CO_2 reduction

ABSTRACT

The use of multichannel monoliths for CO_2 photoreduction applications is gaining increased attention over slurry and annular reactors due to their tunable geometry for reactor designs and exposed surface area per volume. Metal based TiO_2 sol with varying concentrations of Cr, V and Co were deposited on ceramic honeycomb monolithic structures threaded with optical fibres, which can provide light irradiation along each coated interconnected monolithic channel. The coated monoliths show a red shift of absorption edge and light absorption in the visible light region increase with increasing metal concentration compared to pure TiO_2. Photocatalytic activities of the metal based TiO_2 monoliths under visible light irradiation were evaluated for vapour-phase CO_2 photoreduction with H_2O. Maximum acetaldehyde rate of 11.13 $\mu mol/g_{cat}$ h was achieved over the 0.5 wt% V–TiO_2 monolith after 4 h of visible light irradiation.

1. Introduction

The continuous combustion of fossil fuels and depletion of existing resources are intensifying the research and development of alternative future energy options that can directly abate and process ever-increasing carbon dioxide (CO_2) emissions. Over the past decade, titanium dioxide (TiO_2) has been considered to be a promising material for photocatalysis applications due to its chemical stability, nontoxicity and low cost [1,2]. Currently, the time-consuming and costly process of separating and regenerating powder TiO_2 catalyst is a key limitation for slurry reactor designs used in industrial applications. Immobilization of TiO_2 on fixed substrates eliminates post treatment separation and minimizes light loss caused by scattering and absorption of the resulting solution and reactor [3]. Selection of appropriate photocatalytic supports that can optimise the interaction between the anchored TiO_2 photocatalyst, reactants and light is crucial for the development of efficient fixed bed reactor designs for CO_2 photoreduction in both liquid and gas phase applications. The use of multichannel monoliths for photocatalysis applications is gaining increased attention over slurry and annular reactors due to its tunable

* Corresponding author. Tel.: +44 131 451 4737.
E-mail address: O.O.Ola@hw.ac.uk (O. Ola).

http://dx.doi.org/10.1016/j.cej.2015.07.090
1385-8947/

geometry for reactor and catalyst designs and exposed surface area per volume. Monolithic substrates usually made of plastic, metal or ceramic materials have uniform parallel channels upon which thick or thin catalyst films can be deposited on the surface or within the substrate. The dimensions and amount of channels and wall thickness determine the geometric surface area upon which the catalyst is deposited [4]. Applications using monolithic structures for photodegradation of organic compounds [5–7] and UV light induced photocatalytic CO_2 reduction [8–10] have been reported. Monoliths are usually pre-coated with an inorganic oxide prior to coating active catalytic material to ensure good bonding between the monolith and catalyst and prevent catalytic material from being embedded within the macroporous structure of the monolith after calcination. Different types of metal oxides and mesoporous materials have been immobilized on TiO_2 coated monolithic materials to improve photocatalytic activity and light absorption [8–11]. For example, Tahir and Amin [12] prepared montmorillonite (MMT) based TiO_2 monoliths for CO_2 photoreduction with H_2O under UV irradiation. The addition of MMT into TiO_2 matrix was reported to increase surface area with smaller particle size. The main drawbacks associated with catalyst immobilized on multichannel monolithic substrates include limited accessibility of the catalytic surface to photons and reactants and reduced active sites of catalysts due to insufficient light penetration [13,14]. In a model developed by Hossain et al. [15] for influx of UV light within a square channel monolith, half of the incoming light flux was reported to be lost due to light shadowing effect at the entrance of the channel of the monolith wall. The UV light flux was also reported to decrease sharply with increasing distance in the monolith channel. A strategy for improving light distribution in monolithic structures was originally proposed by Du et al. [6], where non coated side-light emitting fibres were evenly distributed in each TiO_2 coated channel to ensure light refracted out of the surface of the fibre could reach the catalyst–reactant interface without attenuation. In recent years, studies on CO_2 reduction using non coated side-light emitting fibres with geometric notches in the core–cladding system were reported to improve photocatalytic activity [3,8–10]. Accordingly, the aim of this study is to optimise the visible light photocatalytic activity of TiO_2 using metal oxide nanomaterials immobilized onto monolithic structures threaded with side-light emitting fibres for CO_2 reduction. Transition metal oxides (V-, Cr- and Co) doped TiO_2 were chosen for this study due to their ability to enhance visible light absorption and photodegradation of organic compounds [16–19]. The coated monolithic structures were further characterized in order to evaluate the influence of these metals on physicochemical properties and photocatalytic activity of TiO_2.

2. Experimental

2.1. Sol preparation and monolith deposition

SiO_2 layer was deposited on cordierite multichannel honeycomb monolith prior to coating with pure TiO_2 or TiO_2 sol with varying metal concentrations (M–TiO_2). This was done to ensure catalyst particles were not ingrained in the macroporous walls of the monolith. Dip-coating method was applied to immobilize SiO_2 sol prepared from a mixture of tetraethyl orthosilicate (Si$(OC_2H_5)_4$, Acros Organics), ethanol (C_2H_5OH, Acros Organics) and dilute hydrochloric acid (HCl, Fisher Scientific) in volume ratios of 2, 2 and 0.04, respectively; on the outer and inner walls of the monolith substrate After two repeated coating cycles of 30 min, the coated monoliths were dried and calcined in a furnace at 973 K for 3 h. SiO_2-coated monoliths were then subsequently immersed in pure TiO_2 or metal based TiO_2 sol prepared using n-butanol, acetic acid, titanium (IV) butoxide and fixed amount of chromium (III) nitrate nonahydrate ($Cr(NO_3)_3{\cdot}9H_2O$, Acros Organics), vanadium (V) oxide (V_2O_5, Fisher Scientific) or cobalt (II) acetylacetonate ($Co(C_5H_7O_2)_2$, Acros Organics) as metal precursors. The initial loading ratios were chosen arbitrarily and then increasing or decreasing ratios were used based on the photocatalytic activities achieved. TiO_2/SiO_2 or M–TiO_2/SiO_2 coated monoliths and resulting sols were dried in a furnace (Carbolite, CWF 1100) under airflow at the rate of 3 K/min to 423 K for 3 h and further calcined to burn off organic compounds and complete crystallization at a heating rate of 5 K/min to 773 K for 1 h. The resulting nanoparticles were pulverized to obtain metal oxide based TiO_2 nanoparticles of varying loading ratios within the range of 0.1–2.0 wt%. Side glowing PMMA optical fibres with geometric notches were cut into the desired length of 6 cm and used as light distribution guides within the coated multichannel monolith.

2.2. Photocatalyst characterization

The crystalline phase and size of the coated monolith samples were examined via powder X-ray diffraction using a Hiltonbrooks X-ray powder diffractometer with Philips PW 1050 goniometer and nickel filtered Cu Kα radiation operating at 20 mA and 40 kV. Samples were scanned within the range of 5–65 (2θ) with scan speed of 2° (2θ) per minute and step size of 0.05. Surface morphology and quantitative analysis were performed using a Quanta 600 model equipped with energy dispersive X-ray (EDX) system and transmission electron microscopy (TEM) on a JEOL 2100F instrument at an acceleration voltage at 200 kV. Pore size distribution of the monoliths were obtained from a mercury (Hg) porosimetry analyser (Micromeritics Autopore IV 9520 V1.05) with Hg pressure in the range of 0.7–275,790 kPa. Specific surface area measurements were estimated from N_2 adsorption–desorption isotherms at 77 K measured using a ChemBET TPR/TPD analyser connected to a linear mass flow controller/gas blender. Chemisorption measurements were conducted with a ChemBET TPR/TPD by injecting pulses of carbon monoxide (CO) gas over the metal coated monoliths to determine metal dispersion. The catalysts were degassed in helium (He) gas stream by raising the temperature at the rate of 10 °C/min at 573 K for 30 min, after which they were reduced by flowing gas stream of 5%H_2/95%N_2 at 673 K for 1 h. The samples were purged and cooled to 323 K in He, and pulse titration was performed using CO at that temperature. CO uptake was measured during titration, from which the metal dispersion was calculated. The elemental ratios and chemical states of the metals contained within the samples were quantified by the Varian Vista MPX ICP-OES (inductively coupled plasma optical emission spectroscopy) system and Kratos AXIS ULTRA with a mono-chromated Al kα X-ray source (1486.6 eV), respectively. The high resolution scans were charge corrected to the main C 1s peak of 285 eV and subsequently quantified to determine the amounts of each element present based on the peak areas, using CASAXPS software with Kratos sensitivity factors. High resolution and wide survey scans were done on each sample. Spectral fitting was performed using CasaXPS software with a line shape based on a Gaussian/Lorentzian mix of 70:30 (GL30). Ultraviolet–visible diffuse reflectance spectroscopy was conducted on the monolith samples using Varian Cary 300 spectrophotometer within wavelength range of 200–800 nm.

2.3. Photoreduction of CO_2

The photocatalytic activities of the monolithic structures coated with pure TiO_2 or Cr, V or Co–TiO_2 were evaluated for CO_2 photoreduction under visible light irradiation. 100 cells per square inch (cpsi) cordierite honeycomb monoliths (Chauger, Taiwan) with

dimensions of 40 mm in diameter and 50 mm in length were used in this study. As shown in Fig. 1, the coated monoliths were threaded with 177 non-coated side light emitting optical fibres to ensure light distribution within the internal channels of the monolith. The reactor was irradiated from the side using a 500 W halogen lamp with wavelength distribution within the range of 400–1100 nm. Pressure and temperature were monitored via a pressure gauge and type T thermocouple, respectively. The reactor was first purged with helium (He) gas to check for leakage and changed to ultra-pure CO_2 (Air Products, 99.9995%) gas saturated with water vapour. The flow of CO_2 saturated with water vapour was continuous throughout the reaction. Gas streams extracted from outlet of the gas-phase photoreactor were analysed using a mass spectrometer (MS, Hiden Analytical) equipped with capillary, quadrupole mass analyser (HAL 201-RC) and Faraday/Secondary electron multiplier (SEM) detectors after 4 h of visible light irradiation.

Each gas compound was determined by using an assigned unique mass and ionization profile. The resulting data were displayed in tabular format as ppm. An average of 3 readings was used from 3 experimental runs. Blank reactions were performed with and without the light source, He and CO_2 in the presence and absence of the catalyst to confirm that reactions were due to CO_2 photoreduction. The presence of hydrocarbons was not identified in the aforementioned conditions.

3. Results and discussion

3.1. Textural properties of coated monoliths

X-ray diffraction patterns of pure TiO_2 and V-, Cr-, and Co-based TiO_2 monoliths are presented in Fig. 2. Diffraction peaks at $2\theta = 25.3°$, 37.8°, 48.1°, 55.1° and 62.7° are ascribed to the (101), (004), (200), (211) and (204) planes of tetragonal anatase TiO_2 (JCPDS Card File No. 65-0191), respectively. This indicates that anatase was the predominant crystalline phase of the coated monolithic structures after calcination at 500 °C. For pure TiO_2, diffraction peaks at ca. 27.4° and 36.1° Correspond to (110) and (101) plane of tetragonal rutile TiO_2 (JCPDS Card File No. 65-0191), respectively. This trend is consistent with as-synthesized sol gel samples reported in the literature [20,21]. Rutile peaks at ca. 27.4° (110) were further observed in the diffraction patterns of 1.5 wt% V–, 2 wt% V– and 2 wt% Cr–TiO_2 monoliths only. The introduction of cations with smaller radii and valence lower than 4, e.g. Co^{2+} or Cr^{3+}, has been reported to accelerate anatase to rutile phase transition due to charge compensation causing the formation of oxygen vacancies that enhance mass transport of atoms in TiO_2 anatase structure [22,23]. Anatase to rutile transformation was promoted at higher metal concentration of Cr and V due to decreased thermal stability of anatase resulting from lattice distortion of anatase by metal incorporation [24,25]. Increase in V concentration promoted increased crystal growth of rutile from 6.96 nm (1.5 wt% V–TiO_2) to 25.12 nm (2 wt% V–TiO_2). No other diffraction peaks in its metal or oxide phase were detected for Cr or Co–TiO_2 monolith samples even at the highest metal concentration of 2 wt%. Absence of the crystal phase of Cr and Co could be due to the occurrence of the metals in highly dispersed amorphous phase within TiO_2 matrix. Absence of the metal or oxide phase in the XRD pattern could be due to their occurrence being in highly dispersed phase within TiO_2 matrix or particle size being too small to be measured within the detectable limit of the diffractometer. Characteristic peaks at 20.3° (001) and 31.0° (400) for orthorhombic vanadium (V) oxide (V_2O_5) (JCPDS Card File No. 42-0876) and 14.9° (110) and 29.9° (220) for tetragonal vanadium (IV) oxide (VO_2) (JCPDS Card File No. 42-0876) were observed in the diffraction pattern of the 2 wt% V–TiO_2 monolith only. This indicates that vanadium species homogeneously nucleate as a separate nano oxide structure with higher metal concentration of 2 wt%. V^{4+} ions can also be easily incorporated into the crystal lattice of TiO_2 substitutionally due to the similarity of its tetragonal crystal structure and ionic radius of 0.63 Å with Ti^{4+} (0.68 Å) [26] when compared to V^{5+} with an ionic radius of 0.59 Å [27] and an orthorhombic or tetragonal pyramidal crystal structure [28]. Furthermore, Gu et al. [26] explained that at lower V doping ratios, the majority of the V^{4+} ions remain in the Ti^{4+} lattice via substitution due to the thermal stability of Ti–O–V linkages. Pure VO_2 phase was also reported to be formed from the excess V^{4+} ions generated from increased metal concentration, while the V_2O_5 phase was formed from the oxidation of VO_2 clusters during calcination [26]. Vanadium in its metal or oxide phase were not observed here in samples with doping ratios <2 wt% either due to the high dispersion of vanadium species in TiO_2 structure or their small particle size [25,29]. The crystalline size of pure and coated TiO_2 monolith samples estimated using the Scherer equation are listed in Table 1. The relative intensities and crystalline size of the metal coated monolithic structures decrease with increased metal concentration when compared to pure TiO_2 monolith. The morphology and elemental composition of TiO_2 coating analysed by SEM–EDS is presented in Fig. 3A and B. Agglomerates of different particle sizes were observed from SEM micrograph using magnification of 6000×. SEM–EDS micrographs confirmed the presence of TiO_2 on the SiO_2 layer. Al and Mg elements are from the monolith which is made of cordierite ($2MgO{\cdot}2Al_2O_3{\cdot}5SiO_2$). Spherical nano-sized

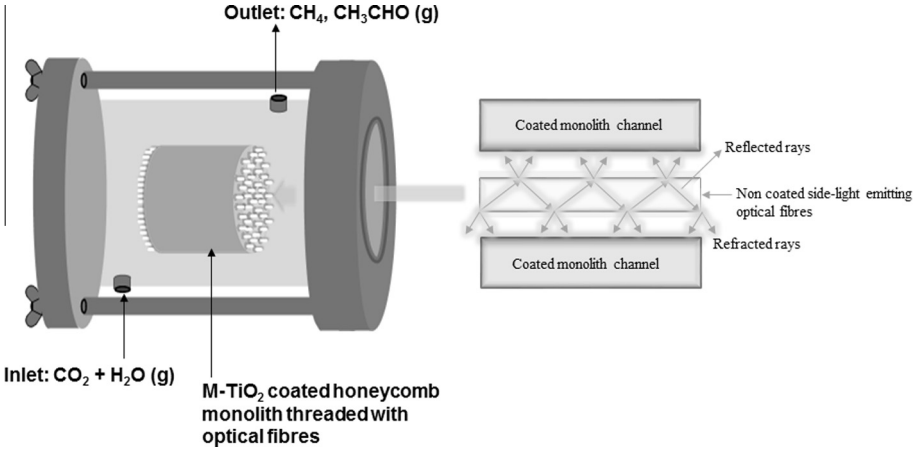

Fig. 1. Schematic of internally illuminated monolith reactor showing light propagation in a channel of a monolith.

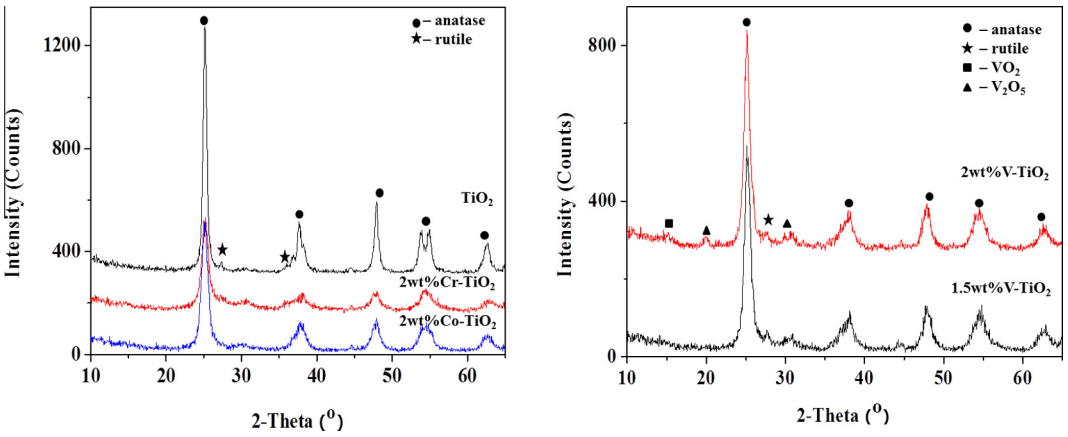

Fig. 2. XRD pattern of monoliths coated with pure TiO_2 and 2 wt% of Cr, V and Co–TiO_2.

Table 1
Characteristics of sol–gel derived monolithic structures coated with pure TiO_2 and different metal concentrations of Cr, V and Co–TiO_2.

Photocatalysts	Crystallite size Anatase (nm)[a]	S_{BET} (m^2/g)[b]	Dispersion (%)[c]	ICP-OES M (%)	XPS
TiO_2	14.92	40.7	–	–	–
0.1 wt% Cr–TiO_2	13.82	91.4	64.22	0.11	0.01
0.5 wt% Cr–TiO_2	13.60	102.9	23.32	0.54	0.03
1.0 wt% Cr–TiO_2	11.81	120.2	13.08	0.95	0.11
1.5 wt% Cr–TiO_2	10.77	119.6	11.76	1.52	0.25
2.0 wt% Cr–TiO_2	10.43	62.2	5.47	1.79	0.37
0.1 wt% V–TiO_2	13.18	97.0	89.69	0.23	0.04
0.5 wt% V–TiO_2	12.88	97.3	74.68	0.52	0.36
1.0 wt% V–TiO_2	12.23	100.2	32.86	1.55	1.90
1.5 wt% V–TiO_2	11.97	118.2	19.59	2.15	2.45
2.0 wt% V–TiO_2	11.33	106.4	11.76	3.96	4.87
0.1 wt% Co–TiO_2	12.06	76.3	89.65	0.10	0.38
0.5 wt% Co–TiO_2	11.89	94.3	62.71	0.47	1.00
1.0 wt% Co–TiO_2	11.26	99.1	30.14	0.96	2.09
1.5 wt% Co–TiO_2	10.24	102.0	24.46	2.22	4.56
2.0 wt% Co–TiO_2	10.06	106.4	19.71	2.60	5.78

[a] Scherrer equation on (101) diffraction peak of anatase TiO_2.
[b] BET surface area.
[c] CO chemisorption, defined as $\delta = M\frac{Na}{L_{Av}} \times \frac{100}{W_S \chi}$ where δ, M, Na, L_{Av}, W_S and χ represents dispersion, molecular weight of metal, number of metal atoms, Avogadro's number, sample mass and metal loading respectively.

particles of varying sizes from 6 to 31 nm were observed from the transmission electron microscopy (TEM) micrographs of pure TiO_2, 2 wt% Cr–TiO_2 (D), 2 wt% V–TiO_2 (E) and 2 wt% Co–TiO_2 monoliths (Fig. 3C–F). The BET specific surface area of the monoliths were within the range of 62.2–120.2 m^2/g (Table 1). Table 1 show that a slight increase in specific surface area of the monoliths coated with Cr, Co and V–TiO_2 occurs when compared to pure TiO_2 monolith (40.7 m^2/g). This may possibly be linked to crystal size which decreases with higher metal concentration and structural changes resulting from the addition of metals. Metal dispersion on the TiO_2 based monoliths was determined by CO chemisorption. At metal concentrations below 2%, metal oxides of Cr, V and Co were found to be present in a dispersed state (Table 1). Dispersion approached almost 90% for Co and V–TiO_2 monoliths at low metal loadings of 0.1 wt%. The dispersion of metal oxide of Cr was 64.22% at 0.1 wt %. Decrease in metal dispersion with higher metal concentration could be due to increasing concentration of metal atoms within TiO_2 framework.

3.2. ICP-OES and XPS analysis

The total elemental composition of metal TiO_2 coated monoliths were determined by ICP-OES, while the chemical state and surface elemental composition were evaluated by XPS. Table 1 lists the metallic content of the coated monoliths quantified by ICP-OES analysis. As shown in Table 1, the surface metal contents for the V and Co–TiO_2 monoliths determined by XPS are higher than their total metal contents while the surface metal content of Cr–TiO_2 monoliths is lower than the total Cr content derived from ICP-OES. This implies that a high concentration of metal ions are primarily located on the surface of V and Co–TiO_2 monoliths while a high concentration of Cr dopant probably migrated to the crystal lattice of TiO_2 during calcination. Table 1 lists the surface elemental composition of the coated monoliths quantified by XPS analysis. The high resolution XPS spectra of the monoliths coated with pure TiO_2 and 2 wt% of Cr, V and Co–TiO_2 are presented in Fig. 4. The binding energies of Ti 2p of pure TiO_2 are at 458.7 eV and 464.5 eV [30,31]. Doublet separation between $2p_{3/2}$ and $2p_{1/2}$ core levels is 5.7 eV. These values are consistent with the values reported in the literature for anatase TiO_2 [28,30]. Ti 2p doublets of 2 wt% Co, V and Cr appear broader and are shifted to higher binding energies compared to the reference position of pure TiO_2. This indicates that chemical state of Ti is influenced by the introduction of metal ions in the TiO_2 crystal lattice [25,32]. Transformation of some Ti ions to higher valence due to the release of electrons in attempt to maintain overall charge might also contribute to shift and broadening of XPS peaks of the metal coated monoliths [33]. The XPS spectra of the O 1s region shows that

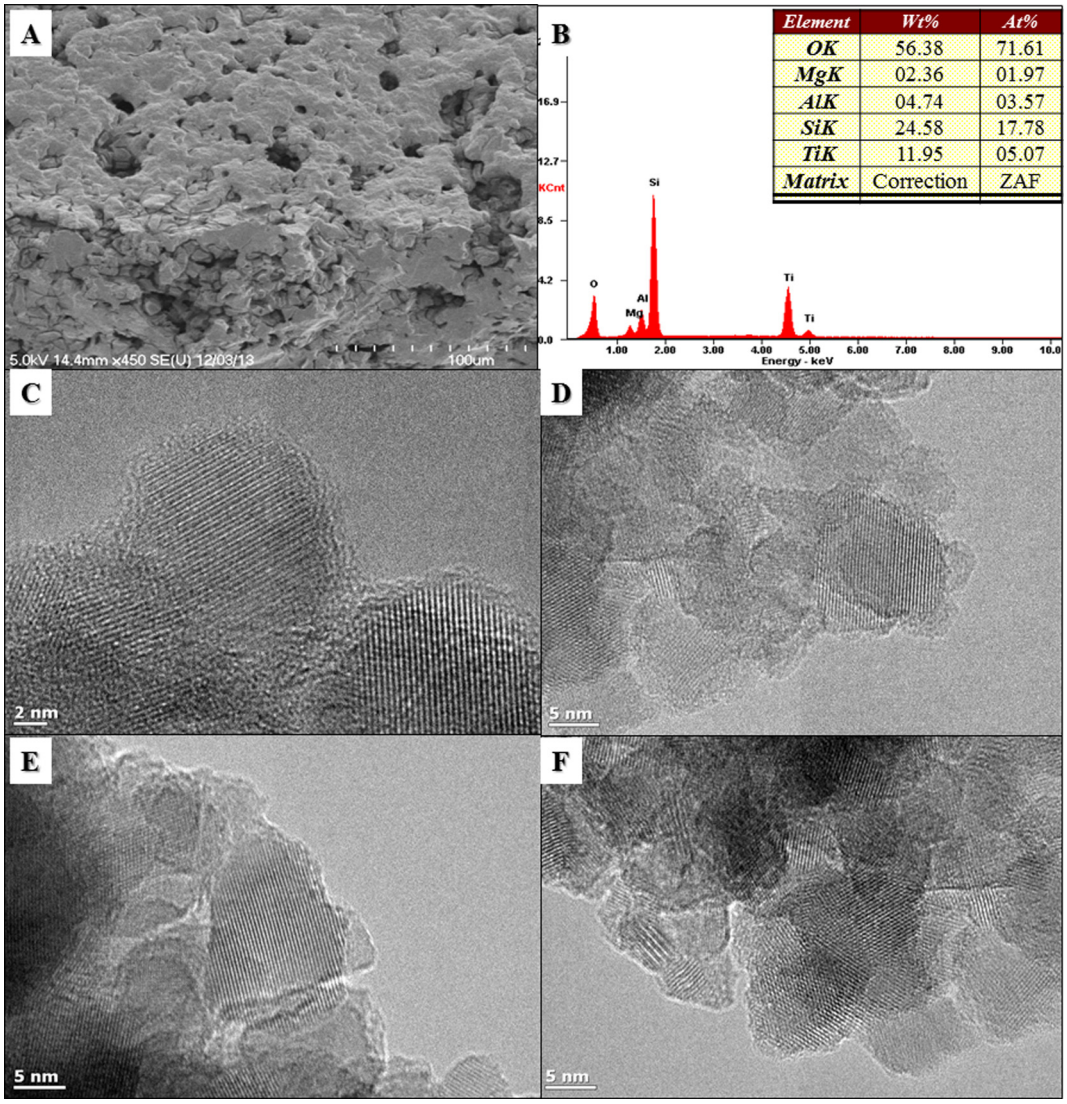

Fig. 3. SEM (A), EDS (B) micrographs of TiO_2 and TEM micrographs of pure TiO_2 (C), 2 wt% Cr–TiO_2 (D), 2 wt% V–TiO_2 (E) and 2 wt% Co–TiO_2 (F) monoliths.

oxygen exists in two forms on the sample surface with binding energies of 530 eV and 531.9 eV. The main peak appears at 530 eV and can be assigned to bulk oxygen bound onto TiO_2. The other peak at 531.9 eV can be attributed to surface oxygen from hydroxyl species on the sample surface [34]. The same phenomenon of peak shift of O 1s to higher binding energies was observed for the metal coated monoliths. Fig. 5 shows that the binding energies of the Cr $2p_{3/2}$ and Cr $2p_{1/2}$ core levels at 576.5 eV and 586.3 eV are characteristic of chromium (III) oxide [30]. For the 2 wt% V–TiO_2 coated monolith, two V $2p_{1/2}$ peaks observed at 524.4 eV and 525.1 eV are characteristic of vanadium (IV) oxide and vanadium (V) oxide, respectively (Fig. 4) [35]. The binding energies of V $2p_{3/2}$ at 516.3 eV and 517.4 eV are also characteristic of vanadium (IV) oxide and vanadium (V) oxide, respectively [28,30]. These values are consistent with the binding energies of V $2p_{3/2}$ measured for V doped TiO_2 [16]. The presence of V^{4+} species in the sol gel derived vanadium doped TiO_2 samples were probably due to the reduction of V^{5+} by the decomposition of organics from starting materials [36,37]. This is supported by the appearance of both V^{4+} and V^{5+} in the XRD pattern of the 2 wt% V–TiO_2 monolith. Detailed analysis of the relative concentrations of V calculated based on the summation of the corresponding peak areas gave a $2p_{3/2}$ and $2p_{1/2}$ abundance equal to 56.9%/12.3% for V^{5+} and 16.3%/14.5% for V^{4+}. This indicates that V^{5+} is the predominate oxidation state with ions mainly present at surface sites at higher concentration compared to V^{4+} which can preferentially occupy TiO_2 lattice sites due to its matching radii. Peaks of Co $2p_{1/2}$ at 796.9 eV and Co $2p_{3/2}$ at 781.2 eV are characteristic of cobalt (II) oxide [30]. The shake-up satellite peaks of Co $2p_{3/2}$ and Co $2p_{1/2}$ which are characteristic of the high spin Co^{2+} are also present at binding energies of 786.1 eV and 802.5 eV, respectively. This indicates that Co species exist in the TiO_2 lattice sites in the form of Co^{2+} [38,39].

3.3. UV–Vis diffuse reflectance spectra of metal coated TiO_2 monoliths

UV–Vis absorbance and diffuse reflectance spectra of monoliths coated with pure TiO_2 and 2 wt% of V, Cr and Co–TiO_2 are presented in Figs. S1 and 5, respectively. The absorption edge of pure TiO_2 monolith is present at 418 nm and corresponds to the band gap energy of 3.0 eV. The band gap energy of the sol gel derived TiO_2 differs from the value of anatase TiO_2 reported in the literature [1]. This difference could be influenced by the method of preparation and presence of rutile confirmed from XRD. Band gap has been reported to be influenced by defect formation i.e. oxygen vacancies during the dehydration of the sol which results in

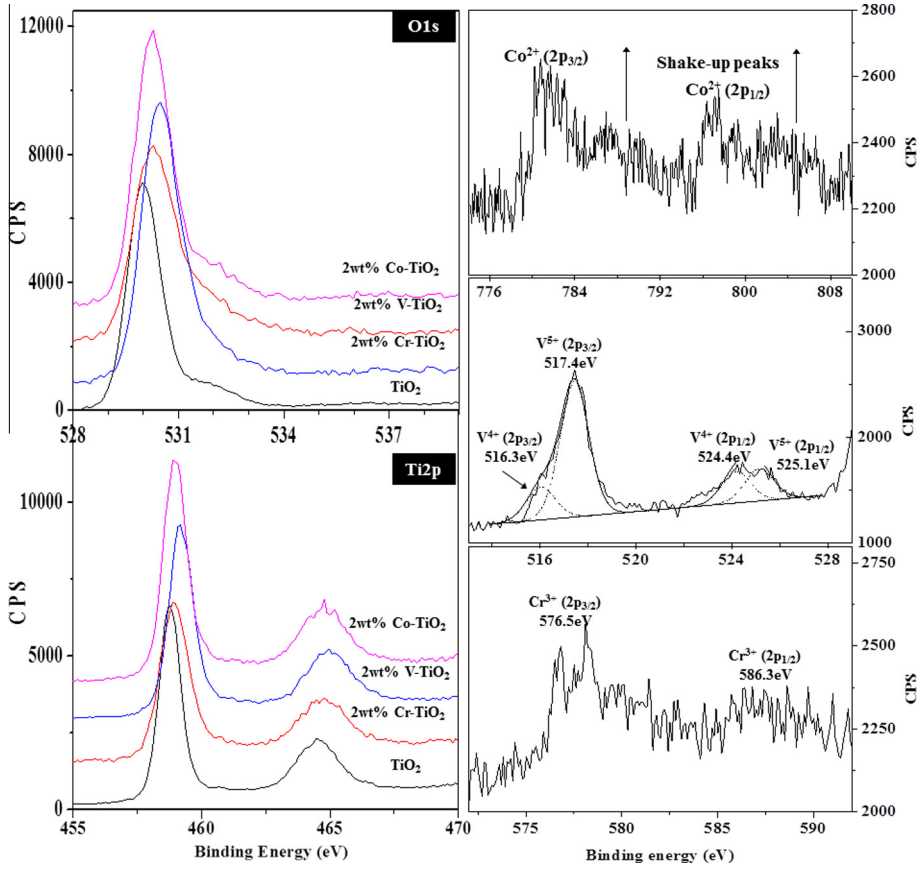

Fig. 4. XPS spectra of monoliths coated with pure TiO_2 and 2 wt% of Cr, V and Co–TiO_2 monoliths.

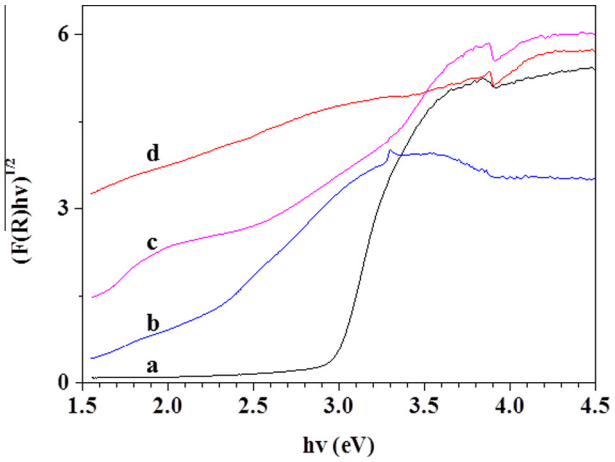

Fig. 5. UV–Vis diffuse reflectance spectra of pure TiO_2 and 2 wt% of V, Cr and Co–TiO_2 monoliths.

stoichiometry deficiency of Ti and O during the sol gel process [40]. Compared to pure TiO_2 monolith, all monoliths coated with V, Cr and Co–TiO_2 have lower band gaps and exhibit increased light absorption in the visible light region. Band gap energy decreased with increasing metal concentration and the highest red shift was observed for the 2 wt% V–TiO_2 monolith (1.9 eV). Visible light absorption has been reported to be due to charge transfer between TiO_2 conduction band and d electrons of the metal dopants [25]. Since the absorption band of V^{4+} and V^{5+} has been reported to be 770 nm and <570 nm [28,37], the formation of an absorption band between 400 and 550 nm for V–TiO_2 monoliths in this present study suggests the presence of both V^{4+} and V^{5+} which is also due to charge transfer transition from O 2p to V 3d orbital at TiO_2 conduction band. The incorporation of Cr^{3+} ions in the TiO_2 matrix is responsible for the shift towards the visible light region with band gap energies of 2.2 eV for 2 wt% Cr–TiO_2 monolith. The tailings observed in the absorption band of Cr–TiO_2 samples have been reported to be assigned to Cr loading creating additional energy levels (Cr 2p level) and oxygen vacancies within the band gap of TiO_2 [31]. Broad absorption band from 540 to 800 nm can be attributed to $^4A_{2g} \rightarrow {}^4T_{2g}$ d–d transition band of Cr^{3+} [41]. Band gap energy of the 2 wt% Co–TiO_2 monolith is 2.3 eV. Broad absorption shoulders formed at 600–800 nm for the 2 wt% Co–TiO_2 monolith is due to the presence of the charge transfer transition between the d orbital of Co 2p to the conduction band of Co^{2+} and this absorption shoulder also increased with higher Co concentration [42].

3.4. Photocatalytic reduction of CO_2

The photocatalytic activities of the monoliths threaded with optical fibres coated with Cr, V and Co–TiO_2 were evaluated for CO_2 photoreduction after 4 h of visible light irradiation (Fig. 6). Trace product formation was observed over pure TiO_2 monolith. Addition of the metal ions improves the photocatalytic activity under visible light irradiation and the metal based TiO_2 monoliths show improved product rates when compared to bare TiO_2 monolith. Visible light photocatalytic activity of the TiO_2 monoliths was influenced by the addition of Cr, V and Co, which is consistent with UV–Vis spectra. As shown in Fig. 6, methane and acetaldehyde formation product rates steadily increase with higher metal concentration to give an optimal ratio of 1 wt% Cr–TiO_2, 0.5 wt%

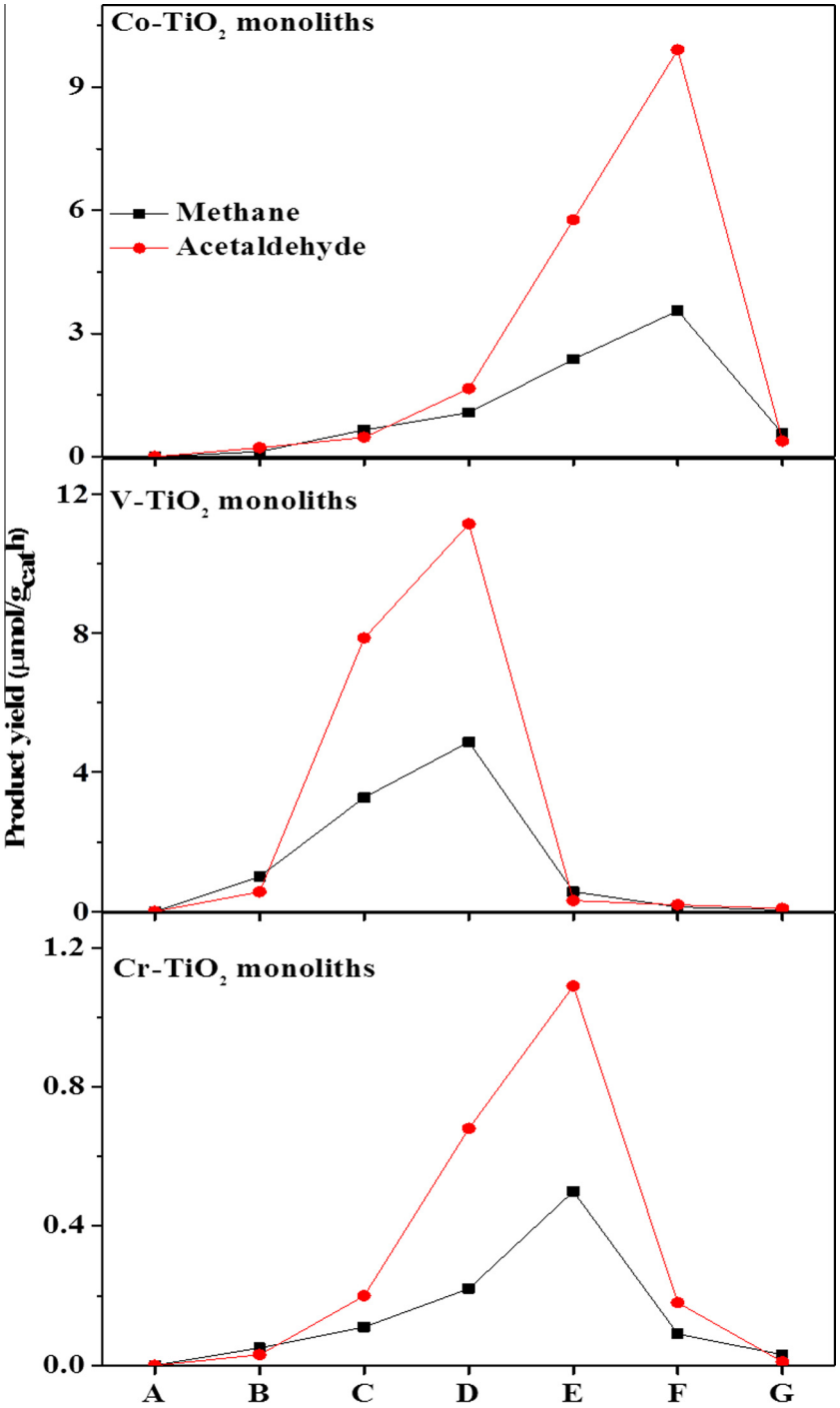

Fig. 6. Product formation rate over metal based TiO_2 monoliths threaded with optical fibres under visible irradiation (A) TiO_2, (B) 0.1 wt% with no optical fibres, (C) 0.1 wt%, (D) 0.5 wt%, (E) 1 wt%, (F) 1.5 wt%, (G) 2 wt%.

V–TiO_2 and 1.5 wt% Co–TiO_2 within the series tested. The effect of irradiation time on the product formation of 1 wt% Cr–TiO_2, 0.5 wt% V–TiO_2 and 1.5 wt% Co–TiO_2 coated monoliths is also presented in Fig. 7. The product rates of the monoliths coated with 0.1 wt% Cr, V and Co–TiO_2 was higher when the monolith threaded with optical fibres was used as a sole support compared to monolithic support without optical fibres. Not all immobilised photocatalyst may be activated when the monolith is used as a lone support due to limited light distribution arising from the catalyst coated on the outer surface absorbing most of the light and light intensity decaying rapidly along the opaque channels of the monolith. The V–TiO_2 monoliths exhibit higher photocatalytic activity for CO_2 reduction with methane and acetaldehyde product rate of 4.87 and 11.13 μmol/g_{cat} h in comparison with other metal coated monoliths; while the lowest activity was observed over Cr–TiO_2 monoliths. The lower product rates can be linked to the dispersion of chromium determined by CO chemisorption. The lowest percentage of exposed metal atoms available for reaction was observed by Cr–TiO_2 monoliths while the highest dispersion rates were observed over the V–TiO_2 monoliths. Thus, the enhanced visible light induced activity of the V–TiO_2 monoliths can be attributed to increased visible light absorption, surface area and

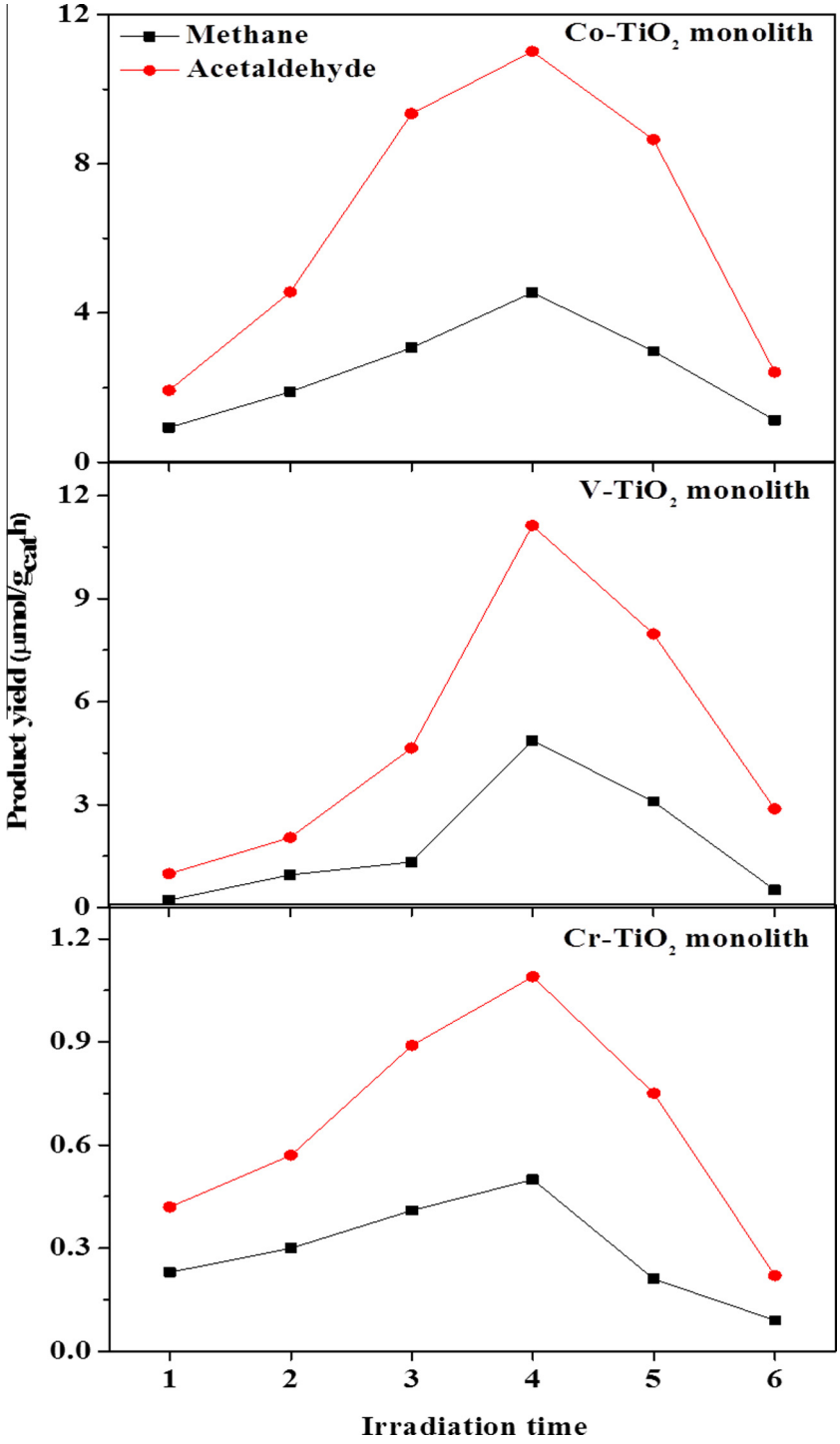

Fig. 7. Effect of irradiation time on product formation over 1 wt% Cr–TiO_2, 0.5 wt% V–TiO_2 and 1.5 wt% Cr–TiO_2 monoliths.

accessible active metal sites arising from the appropriate metal dispersion and loading amount. However, increased metal concentration resulted in reduced product rates over subsequent higher loading ratios. Rutile formation in 1.5 wt% V–, 2 wt% V– and 2 wt % Cr–TiO_2 monoliths can also be a contributing factor in the decline of product formation as the photocatalytic activity of rutile has been reported to be lower than anatase [43]. It can be seen from Fig. 6 that an optimal loading concentration exists for all the metal based monoliths, after which reduced photocatalytic activities were observed. Reduced product rates could be due to the increased level of charge carriers created from the high metal concentration in TiO_2 which limits photocatalytic activity and invariably leads to electron/hole recombination. Decreased metal dispersion observed in Table 1 with increased metal concentration implies that a large percentage of the metal ions are isolated from the surface such that the probability of the trapped charged carriers being transferred to the surface before recombination is low. These results are consistent with the study by Tian et al. [25], where vanadium ions above the optimal loading ratio of 1 wt% resulted in reduced degradation rates of 2, 4-dichlorophenol (2, 4-DCP). The decreased degradation rates were attributed to excess V species reducing surface illumination of catalysts and reducing

the contact area between TiO_2 and the organic pollutant. When the loading content of V exceeded 3 wt%, Wang et al. [44] recorded a decrease in photocatalytic oxidation of 1-phenlethnol due to electron hole recombination. Visible light induced photocatalysis for the metal based monoliths can also be explained via the metal ions influencing electron hole separation when their energy levels satisfy the necessary requirement for CO_2 reduction. For V–TiO_2 monoliths, increased metal concentration predominantly resulted in the formation of V^{5+} ions at the surface layer of TiO_2. An internal electric field was created at the interface of V_2O_5 and TiO_2 during equilibrium due to their p and n-type nature. Diffusion of photogenerated charge carries (electrons and holes) in TiO_2 and V_2O_5 will be induced by this internal electric field such that negative acceptor ions and positive donor ions are left on the p and n side, respectively [45]. Reduced V^{4+} ions can also function as electron and hole traps and participate in reduction reactions with the surface adsorbed species, and thus, preventing electron–hole recombination. Electrons will be transferred from the conduction band of anatase (−0.55 V) to the conduction band of rutile due to the conduction band edge of rutile (−0.35 V) being slightly lower than that of anatase. These photogenerated electrons and holes generated from the interaction of metal species also diffuse to the surface where they accumulate for interfacial charge transfer to adsorbed species. Adsorbed hydrogen and OH radicals are generated from the reaction of H^+ and OH^- ions. Product formation of methane and acetaldehyde then occurs after the reaction of $\cdot CO_2^-$ radicals and ·H with holes. The conduction band edge for V–TiO_2 coated monoliths has been reported to be more negative than the reduction potential of CO_2/CH_4 (−0.24 V) and CO_2/CH_4 (−0.33 V) [46], which indicates that product formation can occur over these monoliths. Valence band edge of Co^{2+} nanocrystals has been reported to lie below the oxygen-evolution potential while the conduction-band edge is above the hydrogen evolution potential of −0.41 V [42]. Band alignment of Co–TiO_2 coated monoliths with redox potentials for methane and acetaldehyde evolution explains product formation reported in Fig. 6. Results from this study are compared to the study of Liou et al. [10] and Tahir and Amin [11] where monolithic structures were employed as catalyst carriers for CO_2 photoreduction. Vapour phase CO_2 with H_2O was reduced to hydrocarbons by $NiO/InTaO_4$ coated monoliths threaded with optical under visible light irradiation. Maximum acetaldehyde conversion rate of 0.3 μmol g^{-1} h^{-1} was achieved with the 2.6% $NiO/InTaO_4$ by simulated sunlight AM1.5G at 70 °C. Recently, In/TiO_2 coated monoliths with two different cell densities and channel lengths were tested for photocatalytic reduction of CO_2 under UV irradiation. The product rates was reported to be influenced by the geometry of the monolith since higher CO and CH_4 production was observed over the monoliths with lower cell density of 100 cpsi and channel length of 2 cm. Maximum product rates were reported to be primarily influenced by higher illuminated surface area to volume ratio in these monoliths as opposed to structures with higher cell densities and lengths. CH_4 production rate of 55.4 μmol g^{-1} h^{-1} was observed over 10 wt% In/TiO_2 monolith with 100cpsi after 10 h of UV irradiation. A comparison between previous results and this present study establishes the effect of catalyst carriers in facilitating improved product formation and light distribution. Results presented here shows higher acetaldehyde product rate when indirectly compared to the experimental results of Liou et al. [10] derived under visible light irradiation. Finally, when comparing this work with the results of Tahir and Amin [11], it should be noted that although both studies chose TiO_2 as semiconductor, different metal dopants, light spectrum, wavelength and intensity were used.

4. Conclusions

Metal based TiO_2 films with varying concentrations of Cr, V and Co were coated on monolithic structures to enhance the photocatalytic reduction of CO_2 using H_2O under visible light irradiation. Compared to pure TiO_2 monolith, all monoliths coated with V, Cr and Co–TiO_2 exhibit lower band gaps and increased light absorption in the visible light region. The V–TiO_2 monoliths exhibit maximum photocatalytic activity for CO_2 reduction while the lowest activity was observed over Cr–TiO_2 monoliths. The lower product rates can be linked to the dispersion of chromium determined by CO chemisorption. Thus, the enhanced visible light induced activity of the metal coated monoliths can be attributed to increased visible light absorption and accessible active metal sites arising from the appropriate metal dispersion and loading amount.

Acknowledgements

The authors thank the financial support provided by the School of Engineering and Physical Sciences and the Centre for Innovation in Carbon Capture and Storage (EPSRC Grant Number EP/K021796/1) at Heriot-Watt University.

Appendix A. Supplementary material

Supplementary data associated with this article can be found, in the online version, at http://dx.doi.org/10.1016/j.cej.2015.07.090.

References

[1] O. Carp, C.L. Huisman, A. Reller, Prog. Solid State Chem. 32 (2004) 33–177.
[2] O. Ola, M.M. Maroto-Valer, J. Photochem. Photobiol. C: Photochem. Rev. 24 (2015) 16–42.
[3] O. Ola, M. Maroto-Valer, D. Liu, S. Mackintosh, C.-W. Lee, J.C. Wu, Appl. Catal. B Environ. 126 (2012) 172–179.
[4] R.M. Heck, S. Gulati, R.J. Farrauto, Chem. Eng. J. 82 (2001) 149–156.
[5] J.T. Carneiro, R. Berger, J.A. Moulijn, G. Mul, Catal. Today 147 (2009) S324–S329.
[6] P. Du, J.T. Carneiro, J.A. Moulijn, G. Mul, Appl. Catal. A: Gen. 334 (2008) 119–128.
[7] H. Lin, K. Valsaraj, J. Appl. Electrochem. 35 (2005) 699–708.
[8] O. Ola, M.M. Maroto-Valer, Catal. Sci. Technol. 4 (2014) 1631–1637.
[9] O. Ola, M. Mercedes Maroto-Valer, J. Catal. 309 (2014) 300–308.
[10] P.-Y. Liou, S.-C. Chen, J.C.S. Wu, D. Liu, S. Mackintosh, M. Maroto-Valer, R. Linforth, Energy Environ. Sci. 4 (2011) 1487–1494.
[11] M. Tahir, N.S. Amin, Appl. Catal. A Gen. 467 (2013) 483–496.
[12] M. Tahir, N.S. Amin, Chem. Eng. J. 230 (2013) 314–327.
[13] D. Chen, F. Li, A.K. Ray, AlChE J. 46 (2000) 1034–1045.
[14] M.N. Chong, B. Jin, C.W.K. Chow, C. Saint, Water Res. 44 (2010) 2997–3027.
[15] M. Hossain, G.B. Raupp, S.O. Hay, T.N. Obee, AlChE J. 45 (1999) 1309–1321.
[16] J.C.-S. Wu, C.-H. Chen, J. Photochem. Photobiol. A 163 (2004) 509–515.
[17] M. Hamadanian, A. Reisi-Vanani, A. Majedi, J. Iran. Chem. Soc. 7 (2010) S52–S58.
[18] S. Zhang, Y. Chen, Y. Yu, H. Wu, S. Wang, B. Zhu, W. Huang, S. Wu, J. Nanopart. Res. 10 (2008) 871–875.
[19] O. Ola, M.M. Maroto-Valer, Appl. Catal. A: Gen. 502 (2015) 114–121.
[20] Y.-H. Zhang, A. Reller, Mater. Sci. Eng.: C 19 (2002) 323–326.
[21] N. Wetchakun, B. Incessungvorn, K. Wetchakun, S. Phanichphant, Mater. Lett. 82 (2012) 195–198.
[22] D.A. Hanaor, C.C. Sorrell, J. Mater. Sci. 46 (2011) 855–874.
[23] S. Riyas, G. Krishnan, P.M. Das, Adv. Appl. Ceram. 106 (2007) 255–264.
[24] G. Zhao, H. Kozuka, H. Lin, T. Yoko, Thin Solid Films 339 (1999) 123–128.
[25] B. Tian, C. Li, F. Gu, H. Jiang, Y. Hu, J. Zhang, Chem. Eng. J. 151 (2009) 220–227.
[26] D.-E. Gu, B.-C. Yang, Y.-D. Hu, Catal. Lett. 118 (2007) 254–259.
[27] L.H. Ahrens, Geochim. Cosmochim. Acta 2 (1952) 155–169.
[28] X. Yang, F. Ma, K. Li, Y. Guo, J. Hu, W. Li, M. Huo, Y. Guo, J. Hazard. Mater. 175 (2010) 429–438.
[29] W. Zhou, Q. Liu, Z. Zhu, J. Zhang, J. Phys. D: Appl. Phys. 43 (2010) 035301.
[30] A.V.N.C.D. Wagner, A. Kraut-Vass, J.W. Allison, C.J. Powell, J.R. Rumble, NIST X-ray Photoelectron Spectroscopy Database 20 Version 4.1, 2012.
[31] Y.-H. Peng, G.-F. Huang, W.-Q. Huang, Adv. Powder Technol. 23 (2012) 8–12.
[32] B. Santara, P. Giri, S. Dhara, K. Imakita, M. Fujii, J. Phys. D: Appl. Phys. 47 (2014) 235304.

[33] J. Zhu, F. Chen, J. Zhang, H. Chen, M. Anpo, J. Photochem. Photobiol. A 180 (2006) 196–204.
[34] R. Chen, H. Liu, J. Chin. Chem. Soc. 58 (2011) 947–954.
[35] K. Bhattacharyya, S. Varma, A. Tripathi, S. Bharadwaj, A. Tyagi, J. Phys. Chem. C 112 (2008) 19102–19112.
[36] S. Liu, T. Xie, Z. Chen, J. Wu, Appl. Surf. Sci. 255 (2009) 8587–8592.
[37] X. Yang, C. Cao, K. Hohn, L. Erickson, R. Maghirang, D. Hamal, K. Klabunde, J. Catal. 252 (2007) 296–302.
[38] C. Huang, X. Liu, Y. Liu, Y. Wang, Chem. Phys. Lett. 432 (2006) 468–472.
[39] C. Shifu, L. Wei, Z. Sujuan, C. Yinghao, J. Sol–Gel Sci. Technol. 54 (2010) 258–267.
[40] E. Sanchez, T. Lopez, Mater. Lett. 25 (1995) 271–275.
[41] B. Tian, C. Li, J. Zhang, Chem. Eng. J. 191 (2012) 402–409.
[42] L. Liao, Q. Zhang, Z. Su, Z. Zhao, Y. Wang, Y. Li, X. Lu, D. Wei, G. Feng, Q. Yu, Nat. Nanotechnol. 9 (2014) 69–73.
[43] L. Liu, H. Zhao, J.M. Andino, Y. Li, ACS Catal. 2 (2012) 1817–1828.
[44] Z.-M. Wang, E. Sahle-Demessie, A. Aly Hassan, J. Nanotechnol. 2011 (2011).
[45] S.-M. Chang, W.-S. Liu, Appl. Catal. B: Environ. 101 (2011) 333–342.
[46] T.F.-R. Shen, M.-H. Lai, T.C.-K. Yang, I.-P. Fu, N.-Y. Liang, W.-T. Chen, J. Taiwan Inst. Chem. E 43 (2012) 95–101.